INSTITUTE OF PHYSICS PUBLISHING JOURNAL OF MICROMECHANICS AND MICROENGINEERING

J. Micromech. Microeng. **16** (2006) 832–842 doi:10.1088/0960-1317/16/4/021

End-coupled optical waveguide MEMS devices in the indium phosphide material system

Marcel W Pruessner[1,2,3,4], **Nathan Siwak**[1,2,3], **Kuldeep Amarnath**[2,3], **S Kanakaraju**[2,3], **Wen-Hsien Chuang**[1,2,3] **and Reza Ghodssi**[1,2,3]

[1] MEMS Sensors and Actuators Lab (MSAL), Department of Electrical and Computer Engineering, A V Williams Building, University of Maryland, College Park, MD 20742, USA
[2] Institute for Systems Research (ISR), University of Maryland, College Park, MD 20742, USA
[3] The Laboratory for Physical Sciences (LPS), 8050 Greenmead Drive, College Park, MD 20740, USA

E-mail: marcelwp@ccs.nrl.navy.mil and ghodssi@eng.umd.edu

Received 31 October 2005, in final form 22 February 2006
Published 20 March 2006
Online at stacks.iop.org/JMM/16/832

Abstract

We demonstrate electrostatically actuated end-coupled optical waveguide devices in the indium phosphide (InP) material system. The design of a suitable layer structure and fabrication process for actuated InP-based waveguide micro-electro-mechanical systems (MEMS) is reviewed. Critical issues for optical design, such as coupling losses, are discussed and their effect on device performance is evaluated. Several end-coupled waveguide devices are demonstrated, including 1×2 optical switches and resonant sensors with integrated optical readout. The 1×2 optical switches exhibit low-voltage operation (<7 V), low crosstalk (−26 dB), reasonable loss (3.2 dB) and switching speed suitable for network restoration applications (140 μs, 2 ms settling time). Experimental characterization of the integrated cantilever waveguide resonant sensors shows high repeatability and accuracy, with a standard deviation as low as $\sigma = 50$ Hz (0.027%) for $f_{\text{resonant}} = 184.969$ kHz. By performing focused-ion beam (FIB) milling on a sensor, a mass sensitivity of $\Delta m/\Delta f = 5.3 \times 10^{-15}$ g Hz^{-1} was measured, which is competitive with other sensors. Resonant frequencies as high as $f = 1.061$ MHz ($Q_{\text{effective}} = 159.7$) have been measured in air with calculated sensitivity $\Delta m/\Delta f = 1.1 \times 10^{-16}$ g Hz^{-1}. Electrostatic tuning of the resonator sensors was also examined. The prospect of developing InP MEMS devices monolithically integrated with active optical components (lasers, LEDs, photodetectors) is discussed.

(Some figures in this article are in colour only in the electronic version)

1. Introduction

Optical micro-electro-mechanical systems (MEMS) generally utilize a 'free-space' approach, in which mirrors direct and modulate the propagation of light. Examples include mirror switches [1], vertical-cavity tunable Fabry–Perot filters for wavelength de-multiplexing [2, 3] and tunable vertical-cavity lasers [4]. While free-space optical MEMS enable low-loss coupling due to the expanded optical mode size (500–1000 μm mirror diameter), monolithic integration with other

[4] Present address: Photonics Technology Branch (Code 5654), Naval Research Laboratory (NRL), Washington, DC 20375, USA.

optical components is difficult and generally requires hybrid packaging, which increases cost.

An alternate method utilizes optical waveguides to confine light on-chip. Such integrated optics [5] enables the monolithic integration of many optical components in a compact and low-cost package. By creating movable and actuated waveguides, the advantages of MEMS (low-power, potential for wavelength and polarization insensitivity, material-independent switching) and integrated waveguides (low loss, tight optical confinement, dense integration) can be realized. Electrostatically actuated optical waveguide switches have been realized with silica waveguides on silicon-on-insulator (SOI) [6], silicon-oxynitride (SiON) [7], polymer [8] and gallium arsenide (GaAs) [9] waveguides. While low-power switching was achieved, the majority of these devices utilized optically passive materials so that on-chip optical gain was not possible.

Although direct band gap GaAs/AlGaAs MEMS [9] enable optical gain, the emission wavelengths are limited to $\lambda < 850$ nm. For optical communications, however, it is desirable to operate at $\lambda = 1550$ nm due to the minimal optical fiber attenuation at this wavelength. Indium phosphide (InP) enables the epitaxial growth of thin-film $In_{1-X}Ga_XAs_YP_{1-Y}$, whose emission wavelength can be tuned from $\lambda_g = 925$ nm (for pure InP) to $\lambda_g = 1670$ nm (for $In_{0.53}Ga_{0.47}As$ lattice matched to InP). For this reason, active research has recently focused on InP-based optical MEMS.

While InP is not traditionally a MEMS material, it is sufficiently robust for micro-mechanical devices [10, 11]; this is especially true for optical applications, in which small displacements are required, typically less than a wavelength ($\lambda \approx 1$ μm). To date, the majority of InP optical MEMS have been free-space tunable filters [2, 3, 12–14] with no demonstration of InP *waveguide* MEMS.

Recently, we demonstrated and characterized suspended InP waveguides for optical MEMS applications [15]. Using this approach, we developed electrostatically actuated in-plane tunable Fabry–Perot filters with integrated waveguides [16]. Optical switches utilizing evanescent coupling between two actuated parallel waveguides were also demonstrated [17]. In this paper, we extend our previous InP MEMS work by demonstrating electrostatically actuated, *end-coupled* optical waveguide switches.

A second application of our end-coupled waveguides concerns sensors. Resonant sensors consist of micro-cantilevers or bridges coated with a receptor film. Adsorption of chemical or biological agents by the receptor results in mass loading and a measurable shift in the resonant frequency. Micro-mechanical resonators were first studied by Nathanson as high Q-factor filters [18]. Howe used a similar device, consisting of a resonant microbridge and CMOS readout circuitry, for vapor sensing [19]. More recently, mercury vapors [20], E. coli cells [21] and explosives have been detected [22] using high-sensitivity off-chip optical detection methods. Using our end-coupled waveguide platform, we demonstrate micro-mechanical resonators with on-chip-integrated waveguides for environmental sensing with optical readout. InP and $In_{1-X}Ga_XAs_YP_{1-Y}$ offer the potential for monolithic integration of optical sources and photodetectors, thereby enabling single-chip sensors to be realized. While the $\lambda = 1550$ nm operating wavelength is not critical for sensing, we chose this wavelength due to our work on end-coupled optical switches for communications applications.

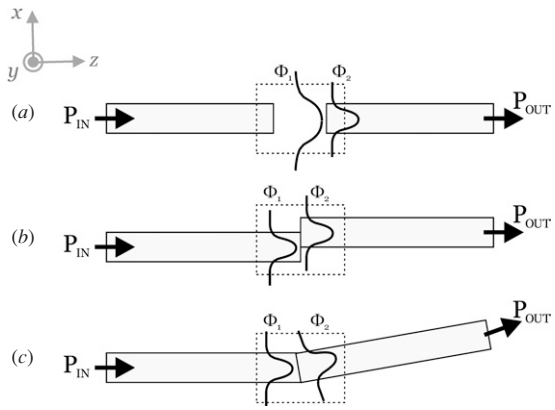

Figure 1. End-coupled waveguides: (*a*) end-separation, (*b*) axial offset and (*c*) angular tilt.

This introduction has reviewed prior work on waveguide and InP MEMS as well as resonant microsensors. In section 2, we review various loss mechanisms between end-coupled optical waveguides, while section 3 reviews the fabrication of InP waveguide MEMS. In section 4, the design and experimental characterization of a 1×2 optical switch for communication networks is presented; section 5 presents the application of our end-coupled waveguide MEMS technology to sensing with integrated optical readout. We then summarize our findings and suggest areas for future work.

2. Theory and design: end-coupled actuated waveguides

2.1. End-coupled waveguides

In the present devices the input waveguide is movable and electrostatically actuated, while the output waveguide(s) is (are) fixed. Figure 1 shows two end-coupled waveguides for three configurations, all of which introduce optical loss: (*a*) end-separation, (*b*) axial offset and (*c*) angular tilt. The losses are analyzed by considering the optical mode-overlap integral for each case. Assuming slab waveguides (confinement in the x-direction and wave propagation in the z-direction), the overlap integral for waveguide end-coupling is [23]

$$T = \left| \int_{-\infty}^{\infty} \phi_1(x)\phi_2(x)\,\mathrm{d}x \right|^2, \qquad (1)$$

where T is the transmittance between input and output waveguide, $\phi_1(x)$ and $\phi_2(x)$ describe the fundamental optical mode field in waveguide 1 and waveguide 2, respectively, and the fields have been normalized such that $\int_{-\infty}^{\infty} |\phi(x)|^2\,\mathrm{d}x = 1$. Identical waveguides with perfect alignment will have maximum coupling, while any difference between the two mode fields (e.g., different waveguides, end-separation, axial offset, angular misalignment, etc) will reduce the transmittance, T.

To compute the coupling losses in figure 1, the fundamental optical mode at $\lambda = 1550$ nm wavelength is

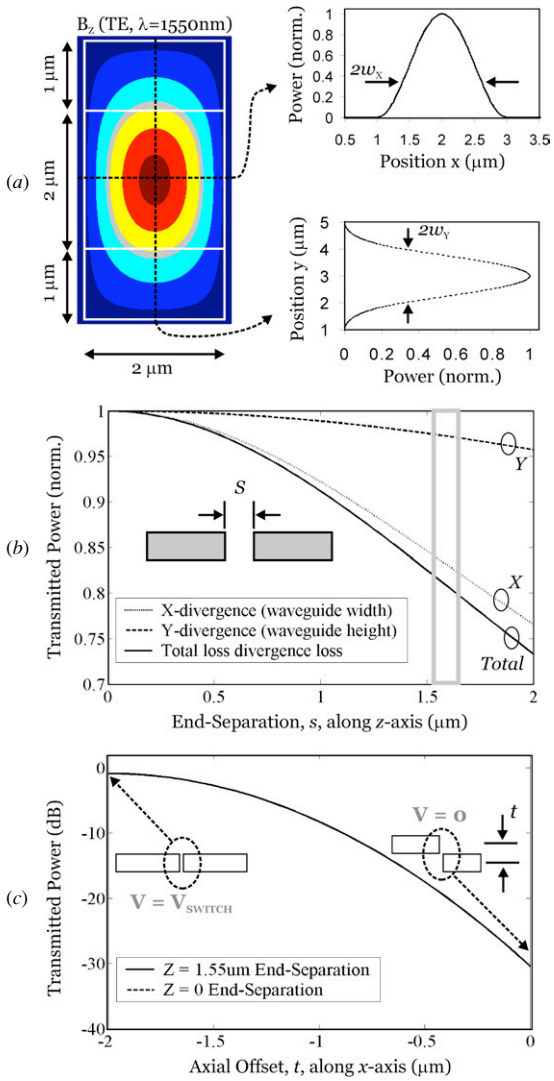

Figure 2. (*a*) Gaussian fundamental mode field diameter simulation, (*b*) end-separation coupling loss due to beam divergence and (*c*) axial offset coupling loss (all simulations: $\lambda = 1550$ nm).

Table 1. Simulated fundamental mode diameter ($2w_X$ and $2w_Y$) for optical switches of width $w = 2$ μm and 2 μm thick core with 1 μm thick top and bottom cladding ($\lambda = 1550$ nm). TE refers to the E-field being perpendicular to the substrate; TM has the E-field parallel to the substrate.

Polarization	Width, w (μm)	Height, h (μm)	Mode: $2w_X$ (μm)	Mode: $2w_Y$ (μm)
TE	2	4	0.77	1.27
TM	2	4	0.83	1.28

simulated using Femlab software (table 1 and figure 2(*a*)). For the simulations, the waveguide core consisted of $In_{0.96}Ga_{0.04}As_{0.08}P_{0.92}$ (refractive index $n = 3.195$, band gap wavelength $\lambda_g = 959$ nm) and the cladding was $In_{0.99}Ga_{0.01}As_{0.01}P_{0.99}$ ($n = 3.173$, $\lambda_g = 925$ nm). We note that λ refers to the optical wavelength in the simulation, while λ_g refers to the band gap wavelength of the semiconductor material. The waveguide had 2 μm width and 4 μm height (figure 2(*a*)). From the simulations, the mode diameter (width) was obtained at the point at which the power drops to $1/e^2$ (electric field drops to $1/e$). Although the polarization of light affects the mode shape, the simulation results in table 1 show only slight deviation in optical mode field diameter, indicating minimal polarization dependence.

Once the mode field diameter is known, the coupling loss is calculated for end-separation, axial offset and angular tilt (figure 1) [23]:

$$T_{\text{end-separation}} = \frac{1}{\sqrt{1 + \left(\frac{z}{n_{\text{cladding}} \cdot k \cdot w^2}\right)^2}}, \tag{2}$$

$$T_{\text{axial-offset}} = \exp\left[-\left(\frac{t}{w}\right)^2\right], \tag{3}$$

$$T_{\text{angular-misalignment}} = \exp\left[-\left(\frac{1}{2} w \cdot n_{\text{cladding}} \cdot k \cdot \alpha\right)^2\right], \tag{4}$$

where z is the end-separation distance, n_{cladding} is the refractive index of the cladding, $k = 2\pi/\lambda$ is the wave vector, $w = w_X$ (or w_Y) is the Gaussian mode field radius (i.e., the diameter is $2w$), t is the axial offset and α is the angular misalignment (in radians, small angle approximation).

2.2. Optical design

The waveguide for these switches is 2 μm wide and 4 μm tall (figure 2(*a*)). After simulation of the mode field, various losses are computed. Due to the rectangular cross section of the waveguide, the beam divergence loss from end-separation is larger along the waveguide width (w_X) than along the waveguide height (w_Y). Each of the divergence losses (w_X and w_Y) is then computed separately and the total loss (transmittance) is then computed, $T_{\text{total}} = T_X T_Y$ (figure 2(*b*)). According to the calculations, the expected total end-separation loss for an $s =$ 1.55 μm air gap is 20% ($T = 80\%$ coupled power).

Figure 2(*c*) shows the coupled power as a function of axial offset. In the switch design, the input and output waveguides are offset axially by 2 μm in the 'OFF' state ($V = 0$), resulting in 30 dB channel isolation. Here, the coupled power is calculated only for displacement along the x-direction (w_X), since the waveguides remain aligned vertically during actuation. At $V = V_{\text{switch}}$, the input and output waveguides are fully aligned and the dominant coupling loss is due to end-separation.

Although the losses calculated in figures 2(*b*) and (*c*) are expected to dominate, there are other issues that need to be considered. For example, the non-verticality of the waveguide sidewalls as a result of dry etching can induce coupling losses. Similarly, fabrication-induced waveguide facet roughness at the semiconductor–air interface can result in scattering and optical loss. Finally, to a lesser extent, interface roughness between the waveguide layers as a result of epitaxial growth can also induce scattering losses. These additional sources of loss will now be considered.

Optical losses at the semiconductor–air interface can result from angular tilt and Fabry–Perot interference due to waveguide facet reflection. These losses, however, are relatively small. Calculations indicate that an $\alpha = 8^\circ$ angular misalignment results in 5% loss. In addition, due to the symmetric actuator design, angular misalignment is expected to be small ($\alpha \ll 8^\circ$), resulting in minimal loss (<5%).

Another concern is facet reflection. Looking at figure 1(*a*), the optical mode traverses two waveguide–air interfaces (waveguide facets). For perfect facets with no roughness, the Fresnel reflected power is $R = |r|^2 = (n_{\text{waveguide}} - 1)^2/(n_{\text{waveguide}} + 1)^2 = 0.27$. These partial mirrors form a Fabry–Perot optical cavity, which results in constructive or destructive interference, depending on the length of the air gap. For air gaps of length $s = N(\lambda/2)$, we have constructive interference (N integer). Therefore, by designing the switches with $s = \lambda = 1550$ nm we ensure constructive interference and minimize Fabry–Perot interference losses.

A related issue concerning facet reflectance is scattering loss due to surface roughness and angled sidewalls. Imaging of the dry-etched waveguide facets has shown surface roughness of $\sigma \leqslant 50$ nm with sidewall verticality of 85° or better. These two factors reduce the Fresnel reflectance significantly. For example, it has been shown that any surface roughness will modify the reflectivity according to [24]

$$r_\sigma = \exp\left[-\frac{1}{2}\left(\frac{4\pi\sigma\cos\theta}{\lambda}\right)^2\right], \tag{5}$$

where σ is the rms mirror surface roughness, $\lambda = 1550$ nm is the wavelength and $\theta \approx 0°$ is the incident angle. The surface roughness in our etch process is $\sigma \approx 50$ nm [17], resulting in a 15% reduction in the facet reflectance, $R_\sigma = R|r_\sigma|^2$, at each waveguide facet. Assuming a single-pass system this results in 30% scattering loss for the two facets. However, multiple reflections in the Fabry–Perot cavity at resonance will increase the total coupled power so that the loss is likely smaller than for the single-pass case. On the other hand, we cannot be assured of perfect alignment of our waveguide facets. Any angular misalignment or curvature of the two waveguide facets will limit the number of reflections within the Fabry–Perot cavity, thereby reducing the coupled power. An estimate of the contribution of facet scattering and facet angle to the total coupling loss is around 20%.

In light of the above considerations, we expect ≈3 dB loss in the end-coupled switches. The two dominant loss contributions are beam divergence as the optical mode traverses the air gap (end-separation) and facet reflection and scattering.

2.3. Electrostatic actuator design

The 1 × 2 switches utilize comb-drive actuators and serpentine suspensions, while the sensors utilize simple cantilever parallel-plate actuators. The 1 × 2 switches were designed as follows. First, the required force for displacing the input waveguide by $\Delta x = 2$ μm (the switching displacement) was simulated using finite-element software (CoventorWare). The force consisted of a pressure load distributed across the 400 μm wide comb-drive region. Analytical equations were used to obtain the comb-drive force as a function of applied voltage for $N = 80$ comb pairs with 1 μm separation between neighboring 2 μm wide comb-fingers. From the simulation (mechanical restoring force) and calculation (electrostatic comb-drive force), the switching voltage for various devices was obtained, resulting in $V_{\text{switch}} = 5$–25 V for devices of length $L = 800$–1600 μm.

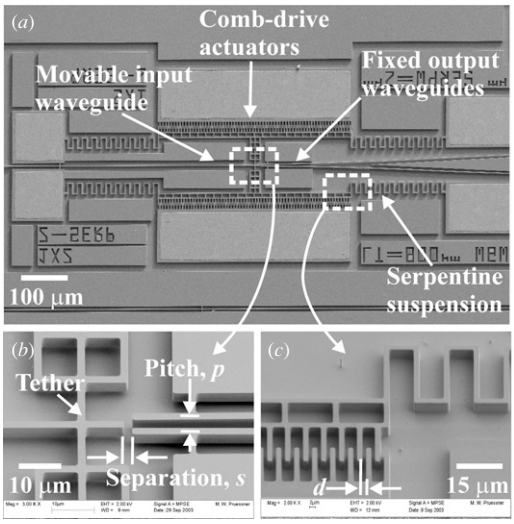

Figure 3. (*a*) End-coupled 1 × 2 switch, (*b*) detail of movable input and fixed output waveguides and (*c*) detail of comb-drive and serpentine suspension. The device length is $L = 800$ μm.

3. Layer structure and fabrication

The device layer structure consisted of an InP substrate (semi-insulating), 1.6–2 μm thick lattice-matched $In_{0.53}Ga_{0.47}As$ sacrificial layer and 1.5–4 μm thick n-doped waveguide layer (the range of thicknesses refer to different sample growths). For the 1 × 2 end-coupled waveguide switches (section 4), the core consisted of 2 μm thick $In_{0.96}Ga_{0.04}As_{0.08}P_{0.92}$ ($n = 3.195$ and $\varepsilon = 0.025\%$) and the top and bottom cladding was 1 μm thick $In_{0.99}Ga_{0.01}As_{0.01}P_{0.99}$ ($n = 3.173$ and $\varepsilon = 0.039\%$). For the cantilever sensors (section 5), the waveguide consisted of a 1.5 μm thick core ($In_{0.96}Ga_{0.04}As_{0.08}P_{0.92}$, $n = 3.195$ and $\varepsilon = 0.025\%$) with air cladding. All layers were grown by solid-source molecular beam epitaxy (MBE). Fabrication of the devices is discussed in our previous work [11, 16, 25] and consists of a two-mask process with methane–hydrogen reactive ion etching (RIE) of InP and sacrificial release in $HF:H_2O_2:H_2O$.

A 1 × 2 end-coupled switch is shown in figure 3 [25]. The device shown utilizes comb-drive actuators and serpentine suspensions for low-voltage switching. The air gap separation between input and output waveguides is $s = 1550$ nm, or one wavelength, and the separation or pitch between the output waveguides is $p = 4$ μm.

4. Experimental: end-coupled 1 × 2 switch

The tested device is as shown in figure 3, but with length $L = 1200$ μm. Lensed fibers coupled optical power into and out of the waveguides ($\lambda = 1550$ nm, TE polarization). We used probes to supply actuation signals to the comb-drives, and a CCD camera was used to image the device during actuation.

4.1. Coupling efficiency

Figure 4 shows the measured coupled power versus dc actuation voltage. At $V = 0$ the input waveguide is not aligned to either output, resulting in 26 dB measured channel

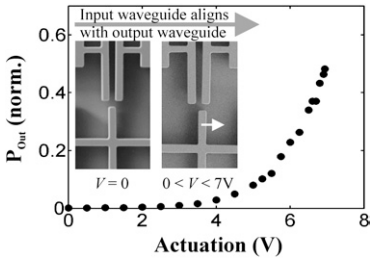

Figure 4. Coupled optical power versus dc actuation voltage in the 1 × 2 switch (λ = 1550 nm, TE).

isolation, close to the 30dB isolation calculated (figure 2(*c*)). The slightly lower measured isolation is likely due to beam divergence across the $s = 1.55$ μm air gap, by which scattered light is coupled to the output. In contrast, the calculation assumes no air gap and hence no beam divergence and scattering.

The maximum coupled power was measured for actuation at $V = 6.9$ V (calculation: 8.6 V). The lower than expected switching voltage is due to fabrication limitations (variation in linewidth of actuator features) and a lower than expected intrinsic tensile material strain. The coupling loss was measured by comparing the maximum coupled optical power of the switch to the coupled power in an identical test waveguide on-chip. Using this approach, the coupling loss was 3.2 dB, which compares favorably with the calculated loss (section 2).

We previously measured a 2.2 dB cm^{-1} waveguide propagation loss using Fabry–Perot contrast and relative power measurements on identical waveguides on a different chip [15]. The 2 μm wide tethers that suspend the waveguides above the substrate (figure 3(*b*)) induce an additional loss of 0.25 dB/tether pair. By reducing the tether width, optimizing the growth and reducing the waveguide doping level ($n = 5 \times 10^{17}/cm^3$), the tether losses and free-carrier absorption losses can be reduced.

4.2. Temporal and frequency response

The end-coupled switch temporal and frequency response were measured as follows. A square wave voltage was applied to the comb-drive causing the input waveguide to align with one of the output waveguides so that coupled optical power was measured. Due to the low-voltage actuator design (large mass comb-drives and compliant serpentine suspensions), the device is mechanically under-damped, resulting in a characteristic 'ringing' in the optical response (figure 5(*a*)). The initial rise time was $T_{RISE} = 140$ μs. However, the ringing decay time increased the steady-state response to $t_{switch} = 2$ ms. Although the switching speed and settling time can be improved by utilizing mechanical stops to prevent oscillation, these mechanical stops have been shown to cause stiction and reliability issues [9]. Furthermore, for network restoration applications, switching speeds of the order of a millisecond are more than sufficient [1] so that the settling time of the present device is reasonable.

The ringing period, T, enables extraction of the damped resonant frequency of the switch, resulting in $f_0 = 1/T = 3.13$ kHz (figure 5(*a*)). Alternatively, the actuator resonant

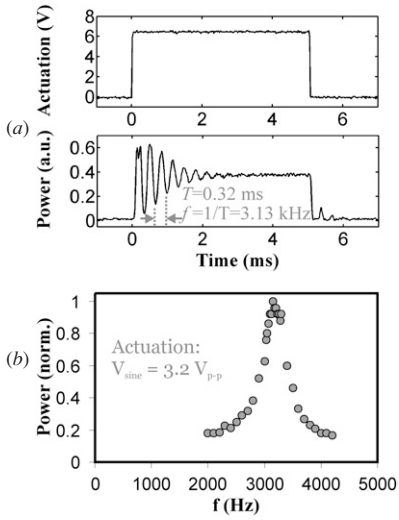

Figure 5. (*a*) Temporal response with square wave actuation and (*b*) frequency response using sinusoidal actuation.

frequency can also be obtained by applying a sinusoidal actuation voltage to the comb-drive. If the actuation frequency matches the resonant frequency of the actuator, then the input waveguide will experience maximum displacement. At maximum displacement, the input and output waveguides will be maximally aligned, resulting in maximum coupled power. Figure 5(*b*) shows such a resonance measurement using a sinusoidal actuation signal (3.2 V_{pp}). The measurement indicates a resonant frequency of $f_0 = 3.2$ kHz, in good agreement with the previous ringing measurement.

4.3. Discussion

The results are the first demonstration of actuated end-coupled optical waveguide MEMS realized entirely in InP-based materials. Although MEMS end-coupled waveguide switches have previously been reported [6–9, 26], the present devices offer the potential for optical gain at λ = 1550 nm. For example, optical sources (LEDs, lasers) and semiconductor optical amplifiers can be monolithically integrated with the MEMS switches, thereby enabling on-chip compensation for optical losses. By taking advantage of the optical absorption (at λ = 1550 nm) of the $In_{0.53}Ga_{0.47}As$ sacrificial layer, pin-photodetectors can be realized as well. Therefore, the InP material system enables us to realize complex transmitter and receiver modules in a monolithically integrated package.

The performance of the optical switch is excellent for most network restoration applications. Low-voltage switching (<7 V) was demonstrated with reasonable loss (3.2 dB), good isolation (26 dB) and moderate switching speed (140 μs, 2 ms settling time). Although the performance is sufficient for network restoration [1], improvements can be made. Currently, the air gap separating input and output waveguides is set to $s = \lambda = 1550$ nm to ensure constructive Fabry–Perot interference, which results in maximum transmission and minimal optical loss. By reducing the gap to $s = \lambda/2 = 775$ nm, end-separation losses due to beam divergence are reduced while still ensuring constructive Fabry–Perot interference. Although this tightens fabrication tolerances, the divergence

losses are expected to be reduced by over 50% (figure 2(*b*)). Second, the temporal response can be improved by utilizing mechanical stoppers to prevent oscillation. Although stiction and reliability are a concern with this approach [9], surface coatings may reduce these effects [27]. Alternatively, complex actuation with acceleration and breaking pulses [9] and active feedback control [28] can be implemented to ensure high speeds and fast settling times in future devices.

5. Resonator sensors

Besides optical communications, our electrostatically actuated end-coupled optical waveguide MEMS technology can also find other applications. In particular, the micro-mechanical waveguides are useful for sensing, as will be shown. In this section, we modify the 1 × 2 end-coupled switches to develop resonant sensors with integrated optical readout. These sensors and the switches from section 4 emphasize the versatility of our InP MEMS waveguide approach in developing devices with a broad range of applications.

5.1. Background

Currently, there is significant interest in developing environmental sensors based on MEMS resonating cantilevers [29]. The cantilevers are coated with a thin receptor film. Adsorption of chemical or biological agents by the receptor results in mass loading and a measurable shift in the cantilever resonant frequency [29]:

$$f_{\text{shifted}} = \frac{1}{2\pi}\sqrt{\frac{3EI}{L^3\,(c_A m_A + c_0 m_0)}}, \tag{6}$$

where E is Young's modulus, I is the cantilever area moment of inertia, L is the cantilever length, m_A is the adsorbed mass, m_0 is the cantilever mass, c_A is a constant that depends on the position of the added mass ($0.24 < c_A < 1$) and $c_0 = 0.24$ is a mass correction factor. From (6) we see that information about specific chemical or biological agents in the environment is obtained by simply measuring the cantilever resonant frequency over time.

To date, the most sensitive measurements utilized external optical detection, which requires large external components (lasers, photodetectors) as well as significant setup and alignment effort. Typically, measurements are performed using an atomic force microscope (AFM) type setup [20], in which a laser beam is focused on the tip of the cantilever and cantilever motion is measured using a position sensitive photodetector [22] to detect the modulated reflected laser beam. Although other detection means including capacitive, piezo-electric, piezo-resistive and electron tunneling techniques have been demonstrated [29], optical detection offers the benefits of high displacement accuracy (nanometers) and relative noise immunity.

The drawback with these optical methods, however, is the need for external optical components (e.g., laser, photodetector), which prohibits the development of compact and portable sensors. Second, there is significant alignment effort associated with an external laser measurement system. Finally, the limited spot size of the laser generally requires cantilever beam widths of several microns, which may result in decreased device sensitivity. Therefore, the development of compact and portable environmental sensors requires a different approach.

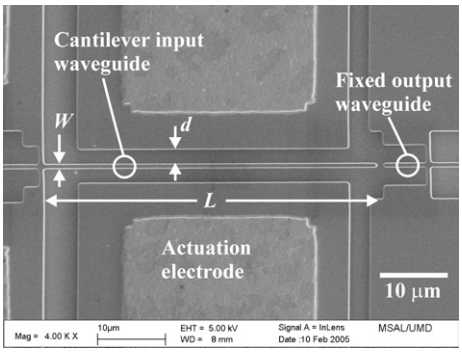

Figure 6. SEM of cantilever resonant environmental sensor with integrated optical waveguides.

Table 2. Mode field diameter ($2w_X$ and $2w_Y$) for two cantilever sensor designs ($\lambda = 1550$ nm, TE).

Design	Width, w (μm)	Height, h (μm)	Mode: $2w_X$ (μm)	Mode: $2w_Y$ (μm)
1	0.6	1.5	0.473	1.154
2	0.8	1.5	0.621	1.143

5.2. Integrated cantilever waveguide resonators

Our sensor consists of a movable cantilever input waveguide end-coupled to a fixed output waveguide [30] (figure 6). The cantilever is actuated to resonance using the side electrodes. By measuring the modulated optical power at the output waveguide, the cantilever resonant frequency is obtained. The advantages of this approach are: (1) the waveguides are self-aligned during fabrication allowing simple device setup for portable applications; (2) the cantilever size can be reduced significantly compared to the external laser approach, resulting in enhanced sensitivity; (3) the choice of InP enables the monolithic integration of optical sources and photodetectors on-chip, thereby allowing true single-chip sensors to be realized.

The sensor design proceeds similar to the 1 × 2 switches. First, the fundamental optical mode is simulated. The sensor waveguides consist of 1.5 μm thick core with air cladding and a waveguide width $w = 0.6$–0.8 μm, resulting in the mode field diameters shown in table 2 ($\lambda = 1550$ nm, TE). Although a detailed loss analysis can be performed, this is not necessary if we are only interested in resonance measurements and not in total coupled optical power. The small mode diameter ($2w_X$) indicates that small displacements ($\leqslant$100 nm) result in measurable changes in coupled output power.

Next, the cantilever resonant frequency is calculated (Young's modulus $E = 80$ GPa [11]). For cantilevers of length $L = 50$–100 μm and width $w = 0.6$–0.8 μm, resonant frequencies $f = 40$–210 kHz are expected. For actuation, the cantilever resonator sensors utilize a simple parallel-plate actuator [18]. Although the resonators were operated far from pull-in, the pull-in voltage gives a useful limit for maximum

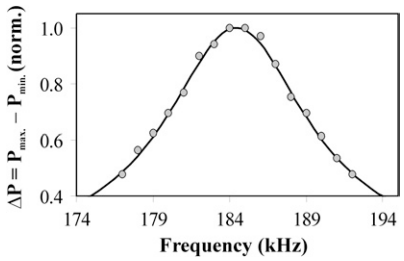

Figure 7. Frequency sweep using a 6 V_{pp} sinusoidal actuation voltage.

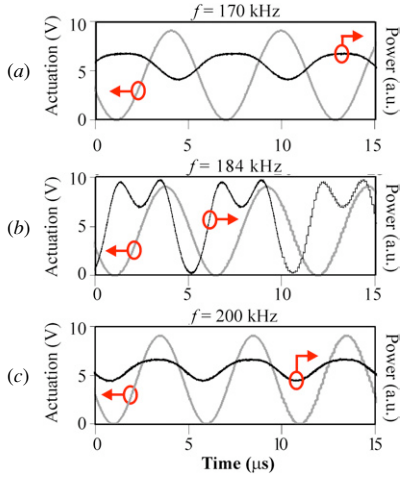

Figure 8. Frequency sweep showing resonant phase shift: (*a*) $f = 170$ kHz ($f < f_0$), (*b*) 184 kHz ($f \approx f_0$) and (*c*) $f = 200$ kHz ($f > f_0$). The dip at resonance in (*b*) is due to the cantilever overshooting its rest position.

operating voltage and displacement. Using standard equations [31], the cantilever sensors were designed for $V_{\text{actuation}} \leqslant 20$ V.

5.3. Resonant frequency measurement

For the sensor experiments, the wavelength was adjusted slightly to obtain maximum coupled power ($\lambda \approx 1550$ nm). The resonant frequency was obtained by actuating the cantilever in-plane (Δx) and measuring the modulated coupled power at the output waveguide. Two approaches can be taken. In the first approach, a sinusoidal actuation voltage is applied to the cantilever while sweeping the frequency. Such a measurement is shown in figure 7 for an $L = 50$ μm, $w = 0.6$ μm cantilever. The resonant frequency is then obtained by fitting a four-parameter Lorentzian line-shape function:

$$A(f) = y_0 + \frac{a}{\left(1 + \left(\frac{f - f_0}{b}\right)^2\right)}, \tag{7}$$

where $A(f)$ is the optical output, f is the frequency, y_0, a and b are curve fit parameters and f_0 is the resonant frequency. The Q-factor is obtained from $Q = f_0/2b$, where we note that this is an effective Q-factor that combines the mechanical Q and the optical response into a single factor.

Figure 8 shows the optical response to a 9.0 V_{pp} sinusoidal actuation voltage for different frequencies. As expected, there is a sharp increase in displacement amplitude at resonance (figure 8(*b*)) compared to the off-resonance conditions

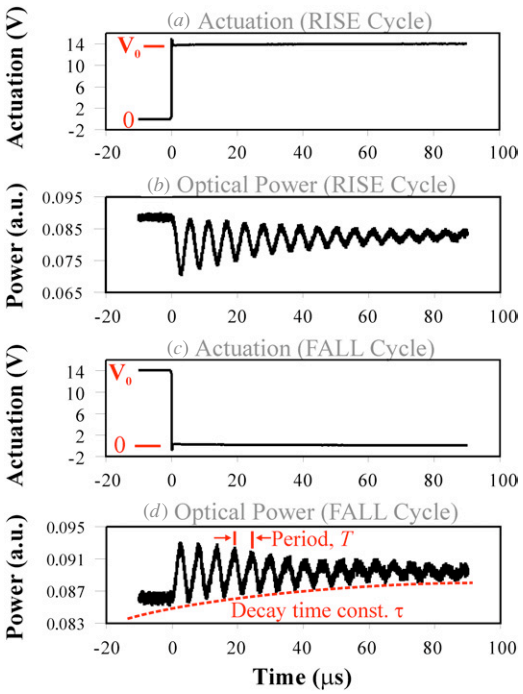

Figure 9. Cantilever ringing experiment: (*a*) actuation (RISE), (*b*) optical ringing (RISE), (*c*) actuation (FALL) and (*d*) optical ringing (FALL).

(figures 8(*a*) and (*c*)). The experiments also illustrate the phase shift characteristic of a linear system as it goes through resonance. For low actuation frequencies ($f < f_0$), the actuation signal and output optical response are $\Delta\phi \approx 180°$ out of phase. Close to resonance ($f \approx f_0$) $\Delta\phi \approx 90°$, while for high actuation frequency ($f > f_0$) the phase angle is $\Delta\phi \approx 0°$. The dip in the optical response at resonance is the result of the cantilever overshooting its rest position (figure 8(*b*)). The results in figure 8 suggest that it is possible to measure resonance not only by considering the amplitude, but also by measuring the phase angle, as was done by Howe [19] for vapor sensing.

Cantilever resonance can also be obtained using a temporal measurement, as in figure 5(*a*). The cantilever is actuated using a square wave voltage signal, resulting in a characteristic optical ringing output (figure 9). We note that the characteristic ringing is present for both the 'RISE' cycle (figures 9(*a*) and (*b*)) as well as the 'FALL' cycle (figures 9(*c*) and (*d*)). However, it is important to be aware of differences in the frequency response for the RISE and FALL cycles, as discussed later. Once the optical ringing data are obtained, the frequency response is extracted as follows. First, the Fast Fourier Transform (FFT) is taken from the temporal ringing data. The result is the unit step response of the cantilever. Next, the magnitude FFT is multiplied by frequency to obtain the impulse response, which gives the true frequency response of the sensor. Finally, a Lorentzian curve fit is performed to obtain the resonant peak (figure 10).

The advantage of this method is that the entire frequency spectrum (fundamental resonant peak) is obtained in a single temporal measurement. In contrast, the frequency sweep method requires many frequency measurements. Furthermore,

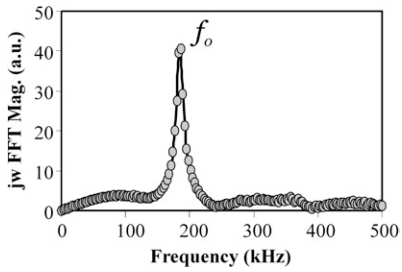

Figure 10. Resonant frequency extraction of FALL optical ringing data by taking the FFT, multiplying by frequency and performing a Lorentzian curve fit.

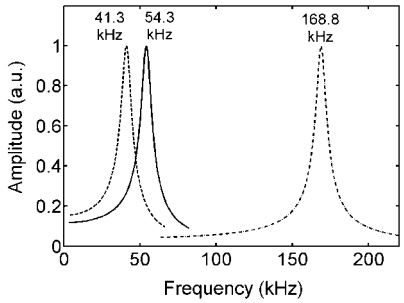

Figure 11. Extracted resonant frequency for three sensors.

due to the periodic nature of the measurement, it is possible to time average the temporal measurement before FFT analysis. This enables high accuracy measurements, even for very small cantilever oscillations of the order of $\Delta x \leqslant 100$ nm.

5.4. Experimental characterization

After development of the measurement and data processing techniques, various experiments were performed to characterize the cantilever sensors. First, the resonant frequency was measured using the ringing method for three devices designated CB-1: $L = 100$ μm, $w = 0.6$ μm, CB-2: $L = 100$ μm, $w = 0.8$ μm and CB-3: $L = 50$ μm, $w = 0.6$ μm (figure 11). The measurements are in good agreement with calculations: $f_{\text{CB-1}} = 41.3$ kHz (calculated: 39.7 kHz), $f_{\text{CB-2}} = 54.3$ kHz (53.0 kHz) and $f_{\text{CB-3}} = 168.8$ kHz (159.0 kHz). The results indicate that the end-coupled cantilever waveguides enable mechanical resonance measurements using on-chip optical detection. The measurements are also very repeatable: a fourth device (type CB-3 on a different chip) gave an average resonant frequency $f_{\text{CB-3,avg.}} = 184.969$ kHz with a standard deviation $\sigma = 50$ Hz (0.027%) over five measurements. The difference in resonant frequency between the two devices of type CB-3 is likely due to fabrication errors in achieving identical linewidths ($w = 0.6$ μm).

Next, a proof-of-concept experiment was performed to determine the ability to measure resonant frequency shifts due to changes in cantilever mass. The resonant frequency of a type CB-2 cantilever ($L = 100$ μm, $w = 0.8$ μm) was measured. We then used a focused-ion beam (FIB) to mill a small mass from a 15 μm long region near the tip of the cantilever. Care was taken not to mill the waveguide facet to avoid excessive scattering losses. The resonant frequency was subsequently re-measured, resulting in a shift $\Delta f = +4.6$ kHz (figure 12).

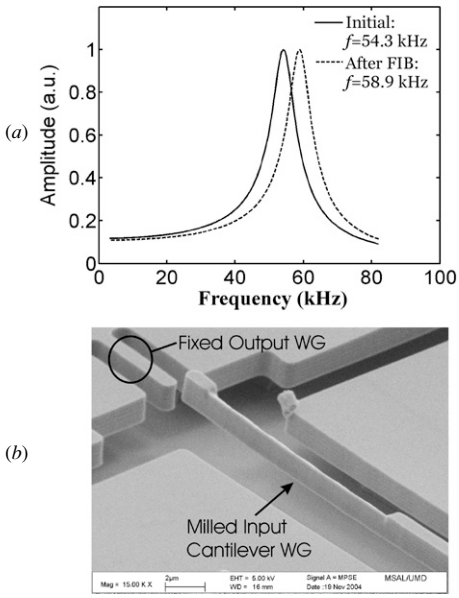

Figure 12. (*a*) Cantilever resonant frequency shift after FIB milling and (*b*) milled input cantilever waveguide.

It is important to note that because mass was removed from the beam ($\Delta m < 0$), the resonance shift is $\Delta f > 0$. In a biochemical sensor utilizing mass loading, the mass shift is $\Delta m > 0$ and $\Delta f < 0$. From Δf the mass change is calculated as $\Delta m = 4.27\%$ of the original beam mass, m_0, or $\Delta m = 2.46 \times 10^{-11}$ g, assuming the change in mass is concentrated at the cantilever free end. The mass-loading sensitivity is [29]

$$\frac{\Delta m}{\Delta f} = \frac{2m_0}{f_0}\frac{c_0}{c_A}, \tag{8}$$

where m_0 is the cantilever mass, f_0 is the resonant frequency, $c_0 \approx 0.24$ is a mass correction factor and $c_0 < c_A < 1$ is determined by the location of the added mass on the cantilever. Using (8), the extracted sensitivity is $\Delta m/\Delta f = 5.3 \times 10^{-15}$ g Hz^{-1}, assuming that the removed mass was confined to the cantilever free end (i.e., $c_A = 1$). Therefore, femtogram-level mass detection is possible with these sensors, competitive with other mass-loading-based resonant sensors [21].

An interesting effect is observed when comparing the RISE and FALL cycle ringing measurements shown in figures 9(*a*)–(*d*) for different square wave amplitudes, V_0. The cantilever is brought to resonance using a parallel-plate capacitive actuator. The total energy in the system is [32]

$$E_{\text{total}} = E_{\text{kinetic}} + E_{\text{capacitor}} \tag{9a}$$

$$\tfrac{1}{2}k_0(\Delta x)^2 = \tfrac{1}{2}k_{\text{effective}}(\Delta x)^2 + \tfrac{1}{2}CV_0^2 \tag{9b}$$

where k_0 is the calculated beam spring constant, Δx is the cantilever beam tip displacement amplitude, C is the actuator capacitance and V_0 is the applied voltage. The measured resonant frequency is the $k_{\text{effective}}$ term, implying that the resonant frequency is a function of the actuation voltage amplitude, V_0 [32]:

$$f_{\text{tuned}}(V) = f_0\sqrt{1 - \frac{\varepsilon A/(d-\Delta x)^3}{k_0}V_0^2}, \tag{10}$$

where ε is the free-space permittivity, A is the electrostatic actuator (capacitor) area and d is the nominal cantilever–electrode separation. Such 'electrostatic tuning' was first

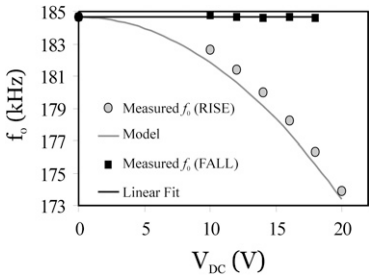

Figure 13. Electrostatic tuning: the RISE cycle is tuned electrostatically while the FALL cycle is invariant to applied V_0.

observed by Nathanson [18]. Figure 13 shows the measured resonant frequency as a function of V_0 for a device type CB-3. The RISE cycle (with $V_0 > 0$) exhibits clear tuning, in agreement with the model. In contrast, the FALL cycle resonant frequency is invariant with actuation amplitude, since $V_0 = 0$ ($f_{0,\text{avg.}} = 184.665$ kHz, standard deviation $\sigma = 59.7$ Hz). The results illustrate the importance of performing the ringing measurements on the FALL cycle, since environmental sensors rely on mass-loading-based frequency shifts, and any electrostatic tuning would skew the measurements.

5.5. Discussion

While the cantilever sensors enable on-chip optical detection of mechanical resonance with demonstrated mass sensitivity of $\Delta m/\Delta f = 5.3 \times 10^{-15}$ g Hz^{-1}, several improvements are possible. First, the optical response as a function of cantilever displacement can be enhanced. Looking at figure 2(*c*), we note that if the two waveguides are initially aligned there is only a small change in the optical response for a given displacement amplitude Δx. However, if we introduce an initial axial offset, x_0, between input and output waveguides, then any cantilever oscillation, Δx, will result in a larger change in optical output, as can be seen by the nonlinear optical response with displacement indicated by the steeper slope in figure 2(*c*). Therefore, higher displacement sensitivity can be realized by introducing an initial axial offset, Δx_0, between input and output waveguides.

By increasing the cantilever resonant frequency, higher sensitivity can be expected. Higher resonant frequency cantilever sensors were fabricated and tested (figure 14). Fundamental resonant frequencies as high as $f = 1.061$ MHz and effective Q-factors as high as $Q_{\text{effective}} = 159.7$ were demonstrated in air, significantly better than our initial devices (figure 11). The results also indicate a distinct $Q \propto f_0^N$ relationship (curve fit: $N = 1.187$) for the Q-factor. Such a relationship was predicted by Hosaka [33] to describe the dependence of squeeze-film damping ($N = 1$) and viscous damping ($0.5 < N < 1$) on cantilever resonant frequency. Based on our results (figure 14(*b*)), we believe the limiting factor is squeeze-film damping and not viscous damping. The slightly higher measured frequency dependence ($N = 1.187$) compared to the model of Hosaka for squeeze-film damping ($N = 1$) is likely the result of the nonlinear optical response of the cantilever versus displacement. In other words, the measured Q-factor is an *effective* Q-factor

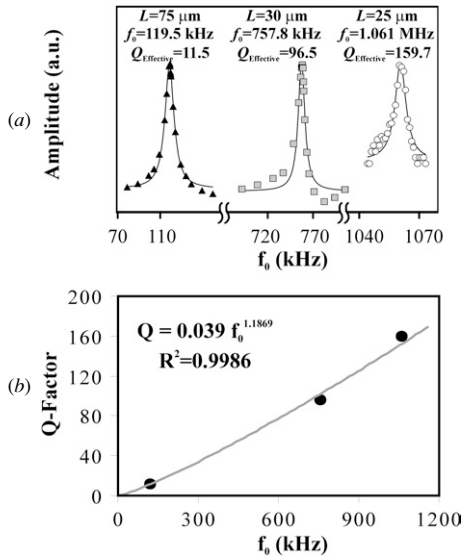

Figure 14. (*a*) Measured resonant frequency and Q-factor for three different cantilevers (2 μm thick core, air cladding and 1 μm waveguide width) and (*b*) extracted Q-factor versus frequency.

combining mechanical and optical responses. Nonetheless, the devices should enable extremely high mass-loading sensitivity, with calculated values as high as $\Delta m/\Delta f = 1.1 \times 10^{-16}$ g Hz^{-1}, assuming mass loading is confined to the cantilever free end (8).

Besides increasing the fundamental resonant frequency of the sensors, the mass-loading sensitivity, $\Delta m/\Delta f$, can also be enhanced by actuating the cantilevers to higher order resonances. The resonant frequency of a vibrational mode n is [34]

$$f_n = \frac{1}{2\pi}\sqrt{\frac{k_0}{m_n^*}}, \tag{11}$$

where k_0 is the cantilever spring constant and m_n^* is the effective mass of the nth vibrational mode. Higher order modes have smaller effective mass, m_n^*, leading to higher resonant frequency, f_n (k_0 remains constant). The smaller effective mass implies that smaller adsorbed masses can be detected, leading to a higher sensitivity. By operating the devices at higher resonant frequencies, air damping is also reduced [33]. Therefore, higher order vibrational modes enable devices with enhanced sensitivity without significant changes in device design.

Future work will focus on functionalizing the cantilevers by coating them with a chemical or biological specific polymer to enable environmental measurements. A second area for future work is to develop integrated single-chip sensors. The existing $In_{0.53}Ga_{0.47}As$ sacrificial layer in the present devices is a good optical absorber at $\lambda = 1550$ nm. Photodetectors can be realized by simply introducing a p–i–n structure using an intrinsic $In_{0.53}Ga_{0.47}As$ layer sandwiched between two doped InP layers, similar to our previous devices [11]. Optical sources (lasers, LEDs) can also be realized by growing an additional active region ($In_{1-X}Ga_XAs_YP_{1-Y}$) on the top of the passive waveguides. Power can then be coupled from the optical source to the passive waveguides, thereby enabling a single-chip integrated sensor.

6. Conclusion

This paper has demonstrated, for the first time, electrostatically actuated end-coupled optical waveguide MEMS devices made of InP-based materials. Optical 1 × 2 switches with low-voltage operation (<7 V), low crosstalk (−26 dB), and reasonable loss (3.2 dB) and switching speed (140 μs, 2 ms settling time) were demonstrated. Future improvements in the optical and the mechanical design of these switches were presented. The end-coupled switches were scaled down to sub-micron waveguide width for application in environmental sensing. An optical ringing technique was implemented to accurately extract the cantilever resonant frequency by measuring the modulated coupled power at the output waveguide. Experimental characterization of the sensors showed that measurements were accurate to a standard deviation as low as $\sigma = 50$ Hz (0.027%) ($f_{\text{CB-3,avg.}} = 184.969$ kHz). By performing focused-ion beam (FIB) milling on a sensor, a mass sensitivity of $\Delta m/\Delta f = 5.3 \times 10^{-15}$ g Hz^{-1} was extracted, which is competitive with other sensors. Resonant frequencies as high as $f = 1.061$ MHz ($Q_{\text{effective}} = 159.7$) have been measured in air with calculated sensitivity as high as $\Delta m/\Delta f = 1.1 \times 10^{-16}$ g Hz^{-1}. Electrostatic tuning of the resonator sensors was also examined. Finally, the prospect of developing true single-chip sensors by taking advantage of the direct band gap of InP-based materials was discussed. Our end-coupled InP waveguide MEMS platform is therefore a versatile technology for integrating micro-optical with micro-mechanical components and can find application in areas ranging from communications to sensing.

Acknowledgments

The authors thank Lynn C Calhoun of the Laboratory for Physical Sciences (LPS) for assistance with the MBE wafer growth, L C Olver for cleanroom access (LPS) and Jonathan McGee for assistance with device fabrication. Professor Ping-Tong Ho gave valuable comments and suggestions, as did Dr Madhumita Datta. This work was generously funded by a National Science Foundation CAREER Award (R Ghodssi), the LPS and by an Achievement Rewards for College Scientists (ARCS) Foundation Fellowship (M Pruessner).

References

[1] Lin L Y, Goldstein E L and Tkach R W 1999 Free-space micromachined optical switches for optical networking *IEEE J. Sel. Top. Quantum Electron.* **5** 4–9

[2] Irmer S, Daleiden J, Rangelov V, Prott C, Römer F, Strassner M, Tarraf A and Hillmer H 2003 Ultralow biased widely continuously tunable Fabry–Pérot filter *IEEE Photon. Technol. Lett.* **15** 434–6

[3] Strassner M, Esnault J C, Leroy L, Leclercq J-L, Garrigues M and Sagnes I 2005 Fabrication of ultrathin and highly flexible InP-based membranes for microoptoelectromechanical systems at 1.55 μm *IEEE Photon. Technol. Lett.* **17** 804–6

[4] Li M Y, Yuen W, Li G S and Chang-Hasnain C J 1998 Top-emitting micromechanical VCSEL with a 31.6 nm tuning range *IEEE Photon. Technol. Lett.* **10** 18–20

[5] Pennings E, Khoe G-D, Smit M K and Staring T 1996 Integrated-optic versus microoptic devices for fiber-optic telecommunication systems: a comparison *IEEE J. Sel. Top. Quantum Electron.* **2** 151–64

[6] Ollier E 2002 Optical MEMS devices based on moving waveguides *IEEE J. Sel. Top. Quantum Electron.* **8** 155–62

[7] Shubin I and Wa P L K 2001 Electrostatically actuated 1 × 2 micromechanical optic switch *Electron. Lett.* **37** 451–2

[8] Bakke T, Tigges C P and Sullivan C T 2002 1 × 2 MOEMS switch based on silicon-on-insulator and polymeric waveguides *Electron. Lett.* **38** 177–8

[9] Bakke T, Tigges C P, Lean J J, Sullivan C T and Spahn O B 2002 Planar microoptomechanical waveguide switches *IEEE J. Sel. Top. Quantum Electron.* **8** 64–72

[10] Greek S *et al* 1997 The strength of indium phosphide based microstructures Proc. *SPIE* **3008** 251–7

[11] Pruessner M W, King T, Kelly D, Grover R, Calhoun L C and Ghodssi R 2003 Mechanical property measurement of InP-based MEMS for optical communications *Sensors Actuators* A **105** 190–200

[12] Daleiden J, Rangelov V, Irmer S, Romer F, Strassner M, Prott C, Tarraf A and Hillmer H 2002 Record tuning range of InP-based multiple air-gap MOEMS filter *Electron. Lett.* **38** 1270–1

[13] Ledantec R, Benyattou T, Guillot G, Spisser A, Seassal C, Leclercq J L, Viktorovitch P, Rondi D and Blondeau R 1999 Tunable microcavity based on InP–air Bragg mirrors *IEEE J. Sel. Top. Quantum Electron.* **5** 111–4

[14] Spisser A, Ledantec R, Seassal C, Leclercq J-L, Benyattou T, Rondi D, Blondeau R, Guillot G and Viktorovitch P 1998 Highly selective and widely tunable 1.55 μm InP/air-gap micromachined Fabry–Perot filter for optical communications *IEEE Photon. Technol. Lett.* **10** 1259–61

[15] Kelly D, Pruessner M W, Amarnath K, Datta M, Kanakaraju S, Calhoun L C and Ghodssi R 2004 Monolithic suspended optical waveguides for InP MEMS *IEEE Photon. Technol. Lett.* **16** 1298–300

[16] Datta M, Pruessner M W, Amarnath K, McGee J, Kanakaraju S and Ghodssi R 2005 Wavelength-selective integrated optical MEMS filter in InP *18th Int. Conf. on Micro Electro Mechanical Systems (Miami Beach, FL)* pp 88–91

[17] Pruessner M W, Amarnath K, Datta M, Kelly D, Kanakaraju S, Ho P-T and Ghodssi R 2005 InP-based optical waveguide MEMS switches with evanescent coupling mechanism *J. Microelectromech. Syst.* **14** 1070–81

[18] Nathanson H C, Newell W E, Wickstrom R A and Davis R J Jr 1967 The resonant gate transistor *IEEE Trans. Electron Devices* **14** 117–33

[19] Howe R T and Muller R S 1986 Resonant microbridge vapor sensor *IEEE Trans. Electron Devices* **33** 499–506

[20] Thundat T, Wachter E A, Sharp S L and Warmack R J 1995 Detection of mercury vapor using resonating microcantilevers *Appl. Phys. Lett.* **66** 1695–7

[21] Ilic B, Czaplewski D, Zalalutdinov M, Craighead H G, Neuzil P, Campagnolo C and Batt C 2001 Single cell detection with micromechanical oscillators *J. Vac. Sci. Technol.* B **19** 2825–8

[22] Pinnaduwage L A, Boiadjiev V, Hawk J E and Thundat T 2003 Sensitive detection of plastic explosives with self-assembled monolayer-coated microcantilevers *Appl. Phys. Lett.* **83** 1471–3

[23] Marcuse D 1986 Tilt, offset, and end-separation loss of lowest-order slab waveguide mode *J. Light. Technol.* **4** 1647–50

[24] Beckmann P and Spizzichino A 1987 *The Scattering of Electromagnetic Waves from Rough Surfaces* (Norwood, MA: Artech House Publishers)

[25] Pruessner M W, Datta M, Amarnath K, Kanakaraju S and Ghodssi R 2005 Indium phosphide based MEMS end-coupled optical waveguide switches *17th Int. Indium*

Phosphide and Related Materials Conference (Glasgow, Scotland) pp 110–3
[26] Ollier E, Labeye P and Revol F 1995 Micro-opto-mechanical switch integrated on silicon *Electron. Lett.* **31** 2003–5
[27] Lim H, Carraro C, Maboudian R, Pruessner M W and Ghodssi R 2004 Chemical and thermal stability of alkanethiol and sulfur passivated InP(1 0 0) *Langmuir* **20** 743–7
[28] Chu P B *et al* 2005 Design and nonlinear servo control of MEMS mirrors and their performance in a large port-count optical switch *J. Microelectromech. Syst.* **14** 261–73
[29] Lavrik N V, Sepaniak M J and Datskosa P G 2004 Cantilever transducers as a platform for chemical and biological sensors *Rev. Sci. Instrum.* **75** 2229–53
[30] Pruessner M W, Chuang W-H, Amarnath K, Kanakaraju S and Ghodssi R 2005 Micromechanical resonators with integrated optical waveguides for sensing applications *Conf. on Lasers and Electro-Optics (Baltimore, MD) (CTuH5)*
[31] Osterberg P M and Senturia S D 1997 M-Test: a test chip for MEMS material property measurement using electrostatically actuated test structures *J. Microelectromech. Syst.* **6** 107–18
[32] Yao J J and MacDonald N C 1996 A micromachined, single-crystal silicon tunable resonator *J. Micromech. Microeng.* **6** 257–64
[33] Hosaka H, Itao K and Kuroda S 1995 Damping characteristics of beam-shaped micro-oscillators *Sensors Actuators A* **49** 87–95
[34] Dohn S, Sandberg R, Svendsen W and Boisen A 2005 Enhanced functionality of cantilever based mass sensors using higher modes and functionalized particles *The 13th Int. Conf. on Solid-State Sensors, Actuators and Microsystems (Transducers) (Seoul, South Korea)* pp 636–9